



Detector of UV light chirality based on a diamond metasurface

JIAJING FENG,^{1,2,3} ZHONGZHU LIANG,^{1,2,3,*} XIAOYAN SHI,¹
YONGJUN DONG,¹ FUMING YANG,^{1,2,3} XIQING ZHANG,¹ RUI DAI,¹
YAN JIA,¹ HUA LIU,¹  AND SIXUAN LI¹

¹Center for Advanced Optoelectronic Functional Materials Research and Key Laboratory of UV Light-Emitting Materials and Technology of Ministry of Education, College of Physics, Northeast Normal University, Changchun 130024, China

²Changchun Institute of Optics, Fine Mechanics and Physics, Chinese Academy of Sciences, Changchun, Jilin, 130033, China

³University of the Chinese Academy of Sciences, Beijing 100049, China

*liangzz@nenu.edu.cn

Abstract: Circularly polarized light (CPL) finds diverse applications in fields such as quantum communications, quantum computing, circular dichroism (CD) spectroscopy, polarization imaging, and sensing. However, conventional techniques for detecting CPL face challenges related to equipment miniaturization, system integration, and high-speed operation. In this study, we propose a novel design that addresses these limitations by employing a quarter waveplate constructed from a diamond metasurface, in combination with a linear polarizer crafted from metallic aluminum. The diamond array, with specific dimensions ($a = 84$ nm, $b = 52$ nm), effectively transforms left-handed and right-handed circularly polarized light into two orthogonally linearly polarized beams who have a polarization degree of approximately 0.9. The aluminum linear polarizer then selectively permits the transmission of these transformed linearly polarized beams. Our proposed design showcases remarkable circular dichroism performance at a wavelength of 280 nm, concurrently maintaining high transmittance and achieving a substantial extinction ratio of 25. Notably, the design attains an ultraviolet wavelength transmission efficiency surpassing 80%. Moreover, our design incorporates a rotation mechanism that enables the differentiation of linearly polarized light and singly circularly polarized light. In essence, this innovative design introduces a fresh paradigm for ultraviolet circularly polarized light detection, offering invaluable insights and references for applications in polarization detection, imaging, biomedical diagnostics, and circular dichroic spectroscopy.

© 2023 Optica Publishing Group under the terms of the [Optica Open Access Publishing Agreement](#)

1. Introduction

Circularly polarized light finds extensive applications in various fields such as quantum communication [1], optical information processing [2,3], circular dichroic spectroscopy [4,5], biological diagnostics [6–8], polarization imaging [9,10], and sensing [11,12]. Therefore, investigating methods to determine the rotational direction of circularly polarized light holds significant scientific importance. In the field of biological diagnostics, many biological molecules and cells exhibit specific circular polarization responses only under ultraviolet (UV) light, making UV circular polarization detection useful for qualitative and quantitative analysis of these substances. Additionally, in quantum communication [1] and optical information processing [2,3], the manipulation and detection of UV circularly polarized light are crucial for achieving efficient photon computing and communication systems. Therefore, researching and developing UV circular polarization detectors have important scientific significance and practical applications. Conventional circular polarization detection techniques rely on bulky optical components such as polarizers, waveplates, and mechanical rotating elements, which limit device miniaturization,

system integration, and high-speed operation. However, with the advancement of micro-nano processing and on-chip technology, on-chip polarization detectors have become the mainstream in the field of polarization detection [13,14]. The fundamental principle of an on-chip polarization detector involves integrating a polarization recognition layer with a photodetector. Typically, the polarization recognition layer consists of a metal polarization grating or a metal micro-nano structure that exhibits distinct transmittance or reflectivity characteristics for incident light with different polarization orientations. As a result, the detector receives varying light intensities, leading to differences in photocurrent magnitude. Chiral organic molecules [15] and perovskites [16] have been reported for circular polarization detection. However, chiral molecules suffer from drawbacks such as slow response times and poor environmental stability. In comparison, metasurface structures offer advantages in terms of fabrication simplicity and compatibility with on-chip manufacturing techniques. Numerous circularly polarized light detectors based on metasurfaces have been reported [17–21]. Nevertheless, these detectors primarily operate within the visible, infrared [22], and terahertz [23] regions, with limited research on circularly polarized light detection in the ultraviolet range. The scarcity of ultraviolet circularly polarized light detectors hampers the advancement and practical utilization of circular polarization detection within this spectral band. Therefore, exploring the application of metasurfaces for UV circular polarization detection is of significant importance for promoting the miniaturization and integration of UV circular polarization detection systems.

This study presents the design of a quarter-wave plate, utilizing a diamond metasurface, and a linear polarizer constructed with metallic aluminum. The design specifically targets the ultraviolet band, focusing on a wavelength of 280 nm. The diamond metasurface is engineered to induce a phase difference of $\pi/2$ upon interaction with incident light. Consequently, this phase manipulation converts incoming left-handed and right-handed circularly polarized light into two beams of linearly polarized light that are mutually orthogonal in terms of their polarization direction. The resulting linearly polarized light exhibits a polarization degree exceeding 0.9. To further enhance the device's capabilities, the linear polarizer, comprised of aluminum metal, selectively impedes the transmission of linearly polarized light parallel to the grating while promoting the transmission of linearly polarized light perpendicular to the grating. This differential transmission behavior gives rise to disparate transmittance characteristics for incident left-handed and right-handed polarized light, facilitating chiral differentiation. The proposed device demonstrates excellent performance, with a transmittance exceeding 80% and an extinction ratio of approximately 25. By achieving these outcomes, our work offers novel insights and inspiration for the advancement of high-efficiency and high-extinction ratio ultraviolet circular polarization detectors.

2. Theoretical analysis

Stomatopoda animals, such as mantis shrimp, possess remarkable visual capabilities owing to their distinctive small-eye structure, enabling them to perceive circularly polarized vision [24,25]. Within each small eye, there exists a reticulated cell at the apex (R8) and seven reticular cells at the base (R1-7). The R8 unit functions as a quarter wave plate (QWP), effectively transforming circularly polarized light (CPL) into linearly polarized light (LPL). Meanwhile, the R1-7 cells, equipped with microvilli, are oriented at a 45° angle relative to the longitudinal axis of the R8 cells, thereby serving as linear grid polarizers (LPs). This configuration allows for the discrimination of LPL with varying orientations, facilitating differential detection of circularly polarized light. Inspired by this intriguing natural design, we have developed a vertically integrated double-layer metasurface design. The proposed structure consists of a diamond nanostructure birefringent metasurface, an aluminum-metal linear polarization nanograting, and a dielectric spacer layer sandwiched between these components. The diamond metasurface functions as a QWP, whereas the aluminum grating serves as an LP.

In the context of propagation along the negative z-axis, a beam of circularly polarized light can be represented as the superposition of two components: x-polarized light and y-polarized light, with a phase difference of $\pi/2$. When this circularly polarized light traverses a quarter-waveplate, the two components experience an additional phase difference of $\pi/2$. Consequently, their phase difference becomes either 0 or π . As a result of this phase manipulation, the combined light resulting from the two components exhibits linear polarization.

In the case of transmissive geometric phase metasurfaces, the transmission characteristics can be described using a Jones matrix [26]:

$$J = \begin{bmatrix} t_u & 0 \\ 0 & t_v \end{bmatrix} \quad (1)$$

where t_u and t_v are the complex transmission coefficients of the incident electromagnetic wave along the main axes u and v of the local coordinate system of the metasurface unit structure, respectively. For a quarter-wave plate, when its fast axis u coincides with the x axis, the Jones matrix is [27]

$$J^* = \begin{bmatrix} 1 & 0 \\ 0 & i \end{bmatrix} \quad (2)$$

Define a rotation matrix:

$$R(\theta) = \begin{bmatrix} \cos \theta & -\sin \theta \\ \sin \theta & \cos \theta \end{bmatrix} \quad (3)$$

θ is the rotation angle of the metasurface rectangular element, and the transfer matrix of the metasurface is [28]:

$$T = R(\theta)JR(-\theta) = \begin{bmatrix} t_u \cos^2 \theta + t_v \sin^2 \theta & (t_u - t_v) \sin \theta \cos \theta \\ (t_u - t_v) \sin \theta \cos \theta & t_u \sin^2 \theta + t_v \cos^2 \theta \end{bmatrix} \quad (4)$$

Then, when $t_u = 1$, $t_v = i$ and left-handed polarized light $E_{LCP} = \frac{1}{\sqrt{2}} \begin{bmatrix} 1 \\ -i \end{bmatrix}$ is incident positively, the output electric field is [29]:

$$E_{\text{out}} = e^{i\theta} \begin{bmatrix} \cos(\theta + \frac{\pi}{4}) \\ \sin(\theta + \frac{\pi}{4}) \end{bmatrix} \quad (5)$$

According to Eq. (5), it can be concluded that the output electric field behaves as linearly polarized light with a polarization angle of $\theta + \frac{\pi}{4}$. Similarly, for right-handed polarized light $E_{RCP} = \frac{1}{\sqrt{2}} \begin{bmatrix} 1 \\ i \end{bmatrix}$, the polarization angle of the linearly polarized light after passing through a quarter of a waveplate is $\theta - \frac{\pi}{4}$.

Based on the effective medium theory, the effective refractive indices of a grating, denoted as n_x and n_y , can be determined for x-polarized light (with the electric field component perpendicular to the grating) and y-polarized light (with the electric field component parallel to the grating),

respectively [30].

$$\begin{cases} n_x = \sqrt{\frac{(n_1 + ik_1)^2(n_2 + ik_2)^2}{f(n_2 + ik_2)^2 + (1-f)(n_1 + ik_1)^2}} \\ n_y = \sqrt{f(n_1 + ik_1)^2 + (1-f)(n_2 + ik_2)^2} \end{cases} \quad (6)$$

Among them, f is the duty cycle of the grating, n_1 , and n_2 are the refractive index of the grating material and the material in the gap between the grating, and k_1 , and k_2 are their corresponding extinction coefficients. To simplify the calculation, the metal is regarded as a perfect conductor, the gap material is air, that is, k_1 tends to infinity, $k_2 = 0$. The effective medium can then be simplified to

$$\begin{cases} n_x = n_2(1-f)^{-1/2} \\ n_y = ik_1\sqrt{f} \end{cases} \quad (7)$$

It is evident that the grating exhibits an equivalent medium that is purely real for X-polarized light. Consequently, the grating can be treated as a dielectric layer, resulting in perfect transmission of light. However, due to the metal not being a perfect conductor, the grating experiences a slight absorption of the incident light, albeit most of the X-polarized light is still transmitted. In contrast, for y-polarized light, only the imaginary part is present, indicating that the grating is equivalent to a metal film. Consequently, most of the y-polarized light is either reflected or absorbed.

3. Structural design

Figure 1 presents a schematic diagram illustrating the element structure of a circular polarization detector designed in this study. The structure comprises a diamond rectangular metasurface and an aluminum wire grating, serving as a quarter wave plate (QWP) and a linear polarizer (LP), respectively. The selection of diamond as the metasurface material is attributed to its high refractive index ($n \sim 2.6$), capability to support Mie resonances, and low losses within the ultraviolet band. Furthermore, established techniques exist for fabricating high-quality nanoscale diamond structures [31,32]. Diamond films with nano-honeycomb structures can be produced by using oxygen plasma etching with porous anodic alumina films as masks [33]. Fabrication of MEMS devices from single crystal diamond using commercial diamond materials and standard cleanroom processes [34]. Diamond nanopillar arrays with high density and uniformity can be fabricated using bias-assisted reactive ion etching in a hydrogen/argon plasma [35].

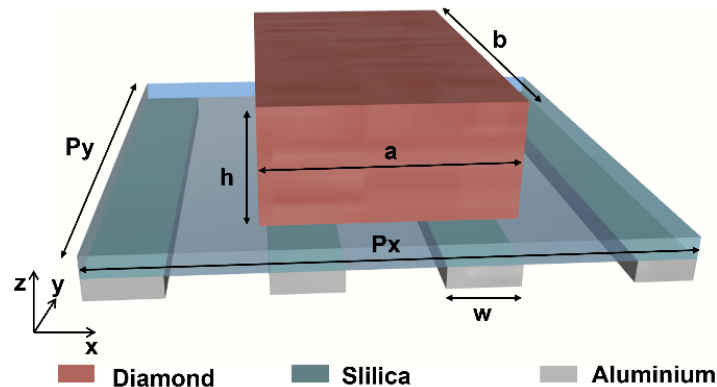


Fig. 1. Schematic diagram of the element structure of a circular polarization detector.

The diamond rectangular columns possess a thickness of $h = 140$ nm, while the periods P_x and P_y are both set at 150 nm. The design principle of the diamond QWP aims to introduce a phase delay of $\pi/2$ for both x-polarized and y-polarized light, which is elaborated upon in the theoretical analysis section. Theoretical analysis reveals that two circularly polarized lights with opposite rotations can exhibit the polarization conversion from circularly polarized to linearly polarized. This conversion is achieved through careful design of the length (a) and width (b) of the diamond rectangular columns. The aluminum LP features a grating width (w) of 10 nm and a grating height of 140 nm. By appropriately selecting the grating width, selective transmission of linearly polarized light that is perpendicular to each other in the two polarization directions is accomplished. A fused silica layer with a thickness of 50 nm is incorporated, and the parameters of the diamond nanopillars and aluminum gratings are optimized using the finite-difference time-domain (FDTD) method. In our simulations, the reflectivity, transmittance, and phase of the device are calculated utilizing the s-parameter analysis group. Periodic boundary conditions are employed on the vertical side of the metasurface element structure, while a perfect match layer (PML) is utilized to truncate the analog domain in the z-axis direction.

4. Analysis of the results

4.1. Design based on a quarter of a wave plate of diamond metasurface

The design process began with the development of the diamond quarter wave plate (QWP), as depicted in Fig. 2. To streamline the design and enhance the performance of the metasurface, an initial step involved maintaining a rotation angle of $\theta=0$, aligning the fast axis u of the metasurface cell with the x-axis direction. Subsequently, the optical properties of the nanopillars were fine-tuned by systematically varying their lengths, and the corresponding complex transmission coefficient was computed for excitation under x-polarized light. During this procedure, the fused silica substrate was treated as a lossless dielectric material with a constant refractive index of $n = 1.45$. To mitigate any substrate resonance effects, the substrate thickness was chosen to exceed the simulation region.

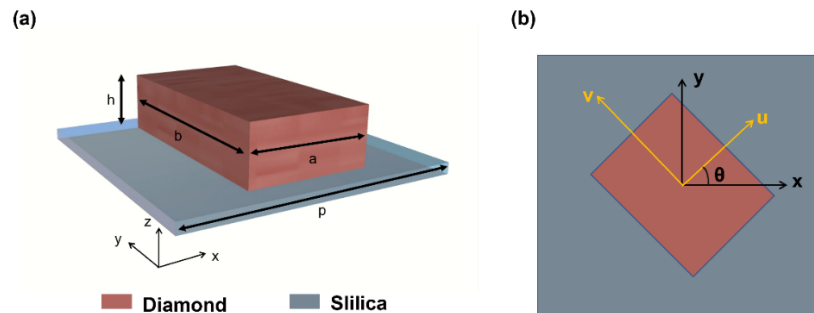


Fig. 2. Schematic diagram of the element structure of a rectangular diamond metasurface.

In the case of incident x-polarized light, we conducted simulations to investigate the relationship between the transmission coefficient (T_{xx}) of the diamond metasurface and the size of the nanopillars at a wavelength of 280 nm. The results of these simulations are presented in Fig. 3(a). Encouragingly, the metasurfaces exhibited a transmission coefficient exceeding 90% across various lengths and widths of the diamond nanopillars. This observation demonstrates the exceptional transmission performance of the diamond metasurface specifically for x-polarized light. The favorable performance can be attributed to the low-loss characteristics of diamond within the ultraviolet range, which holds promise for achieving efficient and precise polarization

control. Consequently, this opens up new prospects for the design and application of optical devices.

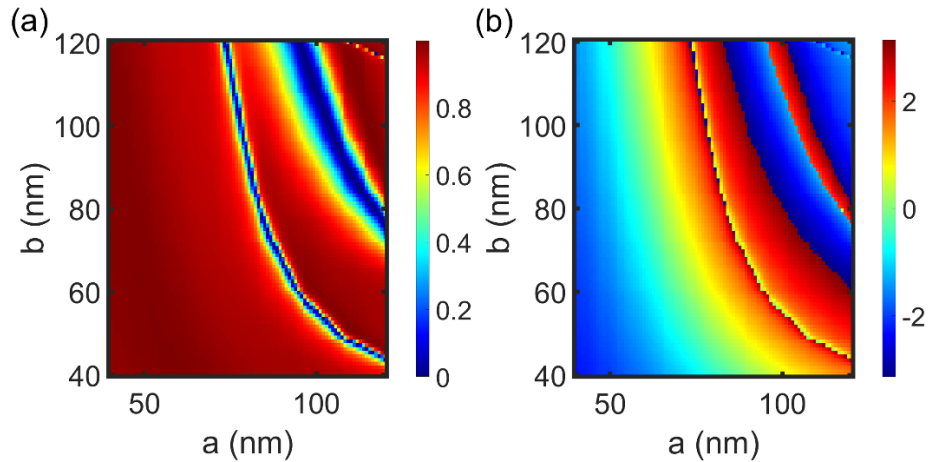


Fig. 3. Variation of (a) transmittance and (b) phase with the length and width of the metasurface under the case of x-polarized light incidence.

Figure 3(b) illustrates our further investigation into the relationship between the phase of x-polarized light upon traversing the diamond metasurface and the dimensions of the diamond rectangular nanocolumn. The results reveal a phase variation range spanning from $-\pi$ to π , indicating the potential for achieving comprehensive phase control by manipulating the size of the diamond nanocolumn. This phenomenon can be ascribed to the alterations in the length and width of the diamond rectangular column, which induce corresponding changes in the effective refractive index of the metasurface. Consequently, the accumulated phase of the transmitted light is adjusted accordingly.

Moreover, we conducted a comprehensive investigation of the behavior of y-polarized light incidence and obtained results similar to those observed for x-polarized light. Remarkably, the diamond metasurface exhibited high transmittance under y-polarized light, demonstrating its effectiveness across different polarization states. Given the element structure's global symmetry along the x and y axes, the complex transmission coefficient T_{yy} for y-polarized light can be accurately predicted by mirroring the amplitude pattern and phase profile of x-polarization along the line $a = b$. This intrinsic symmetry allows us to anticipate the transmittance and phase response of y-polarized light after passing through the metasurface by referencing Fig. 3, as depicted in Fig. 4. By leveraging the phase modulation properties of the diamond metasurface, precise control over the dimensions of the diamond nanopillar enables the attainment of the desired phase modulation, facilitating the realization of an efficient quarter waveplate.

The phase difference $\varphi_{xx} - \varphi_{yy}$, which represents the phase discrepancy between x-polarized light and y-polarized light after traversing the metasurface, is depicted in Fig. 5. Here, φ_{xx} and φ_{yy} denote the respective phases of x-polarized light and y-polarized light. Theoretical analysis indicates that in order to realize a quarter waveplate functionality, the phase difference $\varphi_{xx} - \varphi_{yy}$ should be set to $\pi/2$.

The variation range of $\varphi_{xx} - \varphi_{yy}$ spans from 0 to $3\pi/2$. To achieve a phase difference of $\pi/2$, the point on Fig. 5 corresponding to such a phase difference is chosen, and the corresponding dimensions fulfill the requirements for a 1/4 wave sheet. This determination is made based on the data presented in Fig. 3(a) and Fig. 4(a). It is noteworthy that the majority of length and width data points result in a metasurface transmittance exceeding 90%, with only a small number of regions exhibiting lower efficiency. Therefore, in practical design, it is advisable to avoid

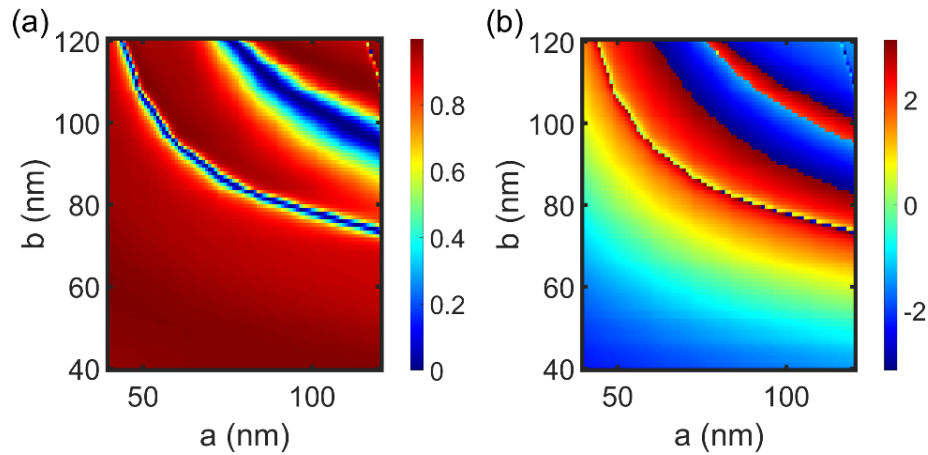


Fig. 4. Variation of (a) transmittance and (b) phase with the length and width of the metasurface under the case of y-polarized light incidence

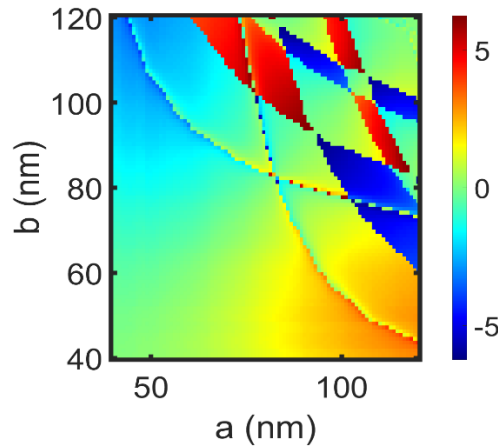


Fig. 5. Phase difference after the incident of x-polarized and y-polarized light vs. diamond length and width.

employing structural parameter combinations associated with low transmission efficiency. For the purpose of simulation verification, we have selected the parameters $a = 84$ nm and $b = 52$ nm.

Under the condition where the angle between the long axis and the x-axis of the metasurface's structural element is 0, we perform simulations to examine the electric field distribution along the z-axis resulting from left-handed and right-handed circularly polarized light interactions with the diamond metasurface. Figure 6 illustrates a three-dimensional schematic representation of the electric field direction.

Degree of polarization serves as a parameter for quantifying the level of alignment in the direction of vibrational motion of a light wave, thereby reflecting the polarization characteristics of light. When dealing with linearly polarized light, the polarization degree assumes a value ranging from 0 to 1. A value of 0 indicates complete lack of polarization (disorder), while a value of 1 signifies complete polarization (order). The degree of linear polarization (DoLP) is

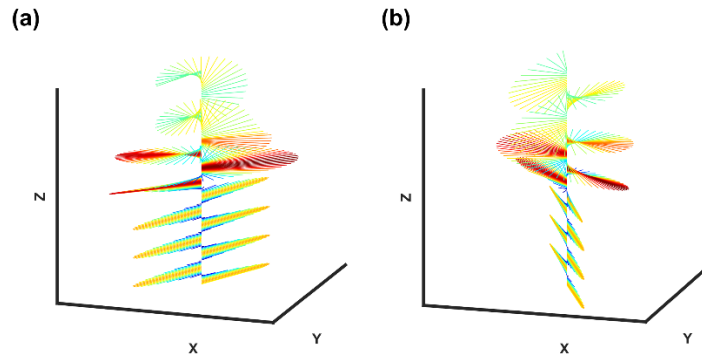


Fig. 6. Electric field distribution on the z-axis of (a) left-handed and (b) right-handed polarized light passing through the diamond metasurface.

determined by:

$$DoLP = \frac{E_x^2 - E_y^2}{E_x^2 + E_y^2} \quad (8)$$

A degree of polarization (DoLP) of 0.9 is computed. It is observed that the circularly polarized light, upon passing through the metasurface, undergoes partial conversion into linearly polarized light, with the polarization directions being mutually perpendicular. As previously analyzed, the polarization angle of the linearly polarized light resulting from left-handed circularly polarized (LCP) incidence is $\pi/4$, while the polarization angle of the linearly polarized light arising from right-handed circularly polarized (RCP) incidence is $-\pi/4$. The simulation outcomes align with the theoretical predictions. Consequently, when the fast axis u of the diamond metasurface unit cell is inclined at an angle of -45 degrees to the x -axis, the converted linearly polarized light obtained from LCP and RCP follows the directions of the x -axis and y -axis, respectively.

4.2. Aluminum grating linear polarizer design

A nanograting polarizer was simulated to replicate the functionalities of a linear polarizer, as depicted in Fig. 7(a). Aluminum was chosen as the material for the designed metal grating, which possesses a period of 50 nm and a grating height of 140 nm. The grating period aligns with the x -axis direction, while its y -axis length is set to infinity. Transmittance simulations were conducted for both x -polarized light and y -polarized light at various grating widths, as illustrated in Fig. 7(b). It can be observed that, with a grating period of 50 nm, the transmittance of both x -polarized light and y -polarized light gradually decreases as the grating width increases. However, the transmittance of polarized light reaches 0 more rapidly compared to x -polarized light. Notably, a substantial transmission disparity between x -polarized and y -polarized light is evident within the grating width range of 8 nm to 20 nm.

By integrating the diamond QWP with the aluminum LP, as depicted in Fig. 1, we validated the functionality of the device. Left-handed and right-handed polarized light were selected as the incident light sources, and the circularly polarized detector recorded the transmitted rates of the left-handed and right-handed polarized light, respectively. This information is presented in Fig. 8. It is evident that our proposed circularly polarized detector is suitable not only for the simulated wavelength of 280 nm but also exhibits periodic changes in transmittance for circularly polarized light within the wavelength range of 250-320 nm. For left-handed circularly polarized light (LCP), the maximum transmittance reaches 90%, whereas for right-handed circularly polarized light (RCP), the transmittance is significantly lower than that of LCP, with a minimum value of 3.5%. The extinction ratio is measured to be 25. These results confirm that our circularly

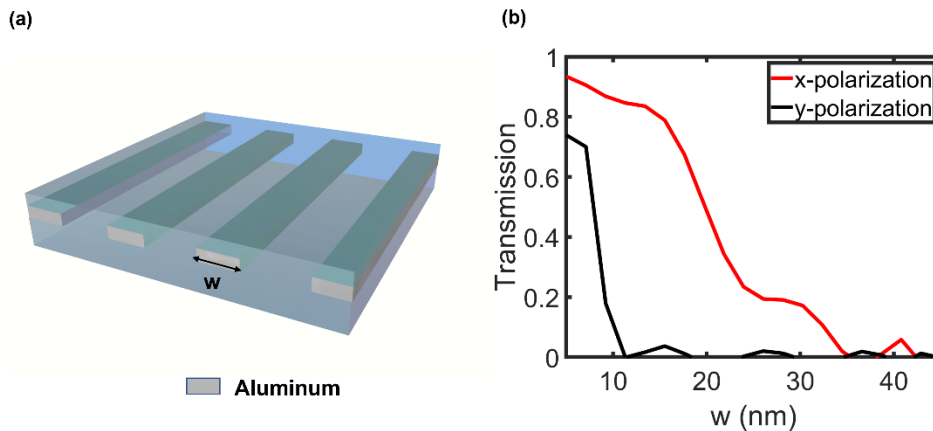


Fig. 7. (a) Schematic diagram of linear polarizer structure (b) Transmittance of gratings for x-polarized light and y-polarized light at different grating widths.

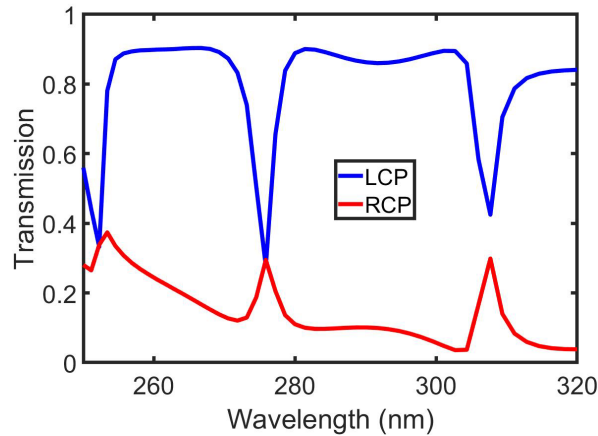


Fig. 8. Transmittance curves for left-handed and right-handed polarized light in the 250-320 nm band.

polarized detector can effectively differentiate the transmittance disparity between left-handed and right-handed polarized light. When a beam of left-handed or right-handed polarized light is incident on our proposed detector, it undergoes conversion to x-polarized or y-polarized light through the diamond metasurface, and subsequently passes through the metal grating polarizer. The transmittance is high if the light is x-polarized, and relatively low if it is y-polarized.

Furthermore, we investigated the disparity in transmittance between linearly polarized light and left-handed circularly polarized light upon passing through the proposed device. To achieve this, we maintained a constant polarization state of the incident light and rotated the unit by 360 degrees. A transmittance monitor was positioned beneath the aluminum LP to capture the transmitted light. The simulation results are presented in Fig. 9.

The observation reveals that as the device undergoes a full rotation, the transmittance of circularly polarized light remains consistently high at 90%. Conversely, the transmittance of linearly polarized light initially decreases from 90% to 10% and subsequently rises back to 90%. This behavior stems from the fact that when circularly polarized light is transformed into linearly polarized light upon passing through the QWP, its polarization direction consistently

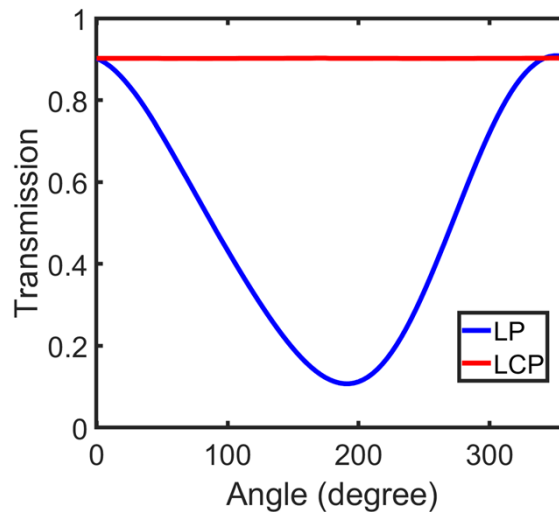


Fig. 9. Transmittance of linearly polarized light (LPL) and left-handed polarized light (LCP) at the rotation angle of different devices.

aligns with the transmission axis of the aluminum grating throughout the rotation. Consequently, the transmittance remains consistently high. Conversely, linearly polarized light, upon passing through the QWP, becomes elliptically polarized light, leading to variations in transmittance after traversing the linear polarizer. This disparity in transmittance enables the detection of both linearly and circularly polarized light.

5. Conclusion

In conclusion, we have developed a circular polarization detector composed of a diamond metasurface-based quarter wave plate (QWP) and an aluminum metal grating linear polarizer. The device demonstrates significant circular dichroism at a wavelength of 280 nm, exhibiting distinct transmittance responses for left-handed and right-handed circularly polarized light. It achieves a remarkable extinction ratio of 25 while maintaining high transmittance, with a maximum transmission efficiency exceeding 80% in the ultraviolet spectral range. Furthermore, the proposed device enables discrimination between linearly and circularly polarized light by observing changes in transmittance upon rotation. This innovative design offers a novel approach for ultraviolet circular polarization detection and holds promise for applications such as ultraviolet polarization detection and imaging, biomolecular diagnostics, and circular dichroic spectroscopy, providing valuable inspiration and references for related fields.

Funding. National Natural Science Foundation of China (61735018); The Science Fund for Distinguished Young Scholars of Jilin Province (20230201080GX); Scientific and Technological Development Project of Jilin Province (20220201080GX); Excellent Member of Youth Innovation Promotion Association of the Chinese Academy of Sciences (Y201836); Leading Talents and Team Project of Scientific and Technological Innovation for Young and Middle-aged Groups in Jilin Province (20190101012JH).

Disclosures. The authors declare no conflicts of interest.

Data availability. Data underlying the results presented in this paper are not publicly available at this time but may be obtained from the authors upon reasonable request.

References

1. W.-L. Zhao, M. Li, H.-Y. Lu, and C.-F. Chen, "Advances in helicene derivatives with circularly polarized luminescence," *Chem. Commun.* **55**(92), 13793–13803 (2019).

2. L. Wesemann, T. J. Davis, and A. Roberts, "Meta-optical and thin film devices for all-optical information processing," *Appl. Phys. Rev.* **8**(3), 1 (2021).
3. L. Kang, C.-Y. Wang, X. Guo, X. Ni, Z. Liu, and D. H. Werner, "Nonlinear chiral meta-mirrors: enabling technology for ultrafast switching of light polarization," *Nano Lett.* **20**(3), 2047–2055 (2020).
4. A. Miles, R. W. Janes, and B. A. Wallace, "Tools and methods for circular dichroism spectroscopy of proteins: A tutorial review," *Chem. Soc. Rev.* **50**(15), 8400–8413 (2021).
5. M. Morgenroth, M. Scholz, T. Lenzer, and K. Oum, "Ultrafast UV–vis transient absorption and circular dichroism spectroscopy of a polyfluorene copolymer showing large chiral induction," *J. Phys. Chem. C* **124**(18), 10192–10200 (2020).
6. D. Ivanov, V. Dremin, A. Bykov, E. Borisova, T. Genova, A. Popov, R. Ossikovski, T. Novikova, and I. Meglinski, "Colon cancer detection by using Poincaré sphere and 2D polarimetric mapping of ex vivo colon samples," *J. Biophotonics* **13**(8), e202000082 (2020).
7. H. J. Butler, J. M. Cameron, C. A. Jenkins, G. Hithell, S. Hume, N. T. Hunt, and M. J. Baker, "Shining a light on clinical spectroscopy: Translation of diagnostic IR, 2D-IR and Raman spectroscopy towards the clinic," *Clinical Spectroscopy* **1**, 100003 (2019).
8. A. M. Kamal, U. M. Pal, A. Kumar, G. R. Das, and H. J. Pandya, "Toward the development of portable light emitting diode-based polarization spectroscopy tools for breast cancer diagnosis," *J. Biophotonics* **15**(3), e202100282 (2022).
9. R. Gao, L. Xu, C. Hao, C. Xu, and H. Kuang, "Circular polarized light activated chiral satellite nanopores for the imaging and analysis of multiple metal ions in living cells," *Angew. Chem.* **131**(12), 3953–3957 (2019).
10. A. E. Woessner, J. D. McGee, J. D. Jones, and K. P. Quinn, "Characterizing differences in the collagen fiber organization of skin wounds using quantitative polarized light imaging," *Wound Rep Reg* **27**(6), 711–714 (2019).
11. H. Han, Y. J. Lee, J. Kyhm, J. S. Jeong, J. H. Han, M. K. Yang, K. M. Lee, Y. Choi, T. H. Yoon, and H. Ju, "High-Performance Circularly Polarized Light-Sensing Near-Infrared Organic Phototransistors for Optoelectronic Cryptographic Primitives," *Adv. Funct. Mater.* **30**(52), 2006236 (2020).
12. P. Grey, S. N. Fernandes, D. Gaspar, E. Fortunato, R. Martins, M. H. Godinho, and L. Pereira, "Field-Effect Transistors on Photonic Cellulose Nanocrystal Solid Electrolyte for Circular Polarized Light Sensing," *Adv. Funct. Mater.* **29**(21), 1805279 (2019).
13. C. Zhang, X. Wang, and L. Qiu, "Circularly polarized photodetectors based on chiral materials: a review," *Front. Chem.* **9**, 711488 (2021).
14. M. Dai, C. Wang, B. Qiang, F. Wang, M. Ye, S. Han, Y. Luo, and Q. J. Wang, "On-chip mid-infrared photothermo-electric detectors for full-Stokes detection," *Nat. Commun.* **13**(1), 4560 (2022).
15. D. Zhu, W. Jiang, Z. Ma, J. Feng, X. Zhan, C. Lu, J. Liu, J. Liu, Y. Hu, and D. Wang, "Organic donor-acceptor heterojunctions for high performance circularly polarized light detection," *Nat. Commun.* **13**(1), 3454 (2022).
16. C. Chen, L. Gao, W. Gao, C. Ge, X. Du, Z. Li, Y. Yang, G. Niu, and J. Tang, "Circularly polarized light detection using chiral hybrid perovskite," *Nat. Commun.* **10**(1), 1927 (2019).
17. C. Zhang, J. Hu, Y. Dong, A. Zeng, H. Huang, and C. Wang, "High efficiency all-dielectric pixelated metasurface for near-infrared full-Stokes polarization detection," *Photonics Res.* **9**(4), 583–589 (2021).
18. A. Basiri, X. Chen, J. Bai, P. Amrollahi, J. Carpenter, Z. Holman, C. Wang, and Y. Yao, "Nature-inspired chiral metasurfaces for circular polarization detection and full-Stokes polarimetric measurements," *Light: Sci. Appl.* **8**(1), 78 (2019).
19. J. Hong, J. van de Groep, N. Lee, S. J. Kim, P. Lalanne, P. G. Kik, and M. L. Brongersma, "Nonlocal metasurface for circularly polarized light detection," *Optica* **10**(1), 134–141 (2023).
20. C. Zheng, J. Li, S. Wang, J. Li, M. Li, H. Zhao, X. Hao, H. Zang, Y. Zhang, and J. Yao, "Optically tunable all-silicon chiral metasurface in terahertz band," *Appl. Phys. Lett.* **118**(5), 051101 (2021).
21. S. J. Li, B. W. Han, Z. Y. Li, X. B. Liu, G. S. Huang, R. Q. Li, and X. Y. Cao, "Transmissive coding metasurface with dual-circularly polarized multi-beam," *Opt. Express* **30**(15), 26362–26376 (2022).
22. Y. Peng, X. Liu, L. Li, Y. Yao, H. Ye, X. Shang, X. Chen, and J. Luo, "Realization of vis–NIR dual-modal circularly polarized light detection in chiral perovskite bulk crystals," *J. Am. Chem. Soc.* **143**(35), 14077–14082 (2021).
23. B. Yang, M. Ouyang, H. Ren, C. Ma, Y. Zhao, Y. Zhang, and Y. Fu, "A Dual-Frequency Terahertz Metasurface Capable of Distinguishing the Handedness of Circularly Polarized Light," *Coatings* **12**(6), 736 (2022).
24. I. M. Daly, M. J. How, J. C. Partridge, S. E. Temple, N. J. Marshall, T. W. Cronin, and N. W. Roberts, "Dynamic polarization vision in mantis shrimps," *Nat. Commun.* **7**(1), 12140 (2016).
25. T. W. Cronin, M. L. Porter, M. J. Bok, R. L. Caldwell, and J. Marshall, "Colour vision in stomatopod crustaceans," *Phil. Trans. R. Soc. B* **377**(1862), 20210278 (2022).
26. Y. Hu, X. Wang, X. Luo, X. Ou, L. Li, Y. Chen, P. Yang, S. Wang, and H. Duan, "All-dielectric metasurfaces for polarization manipulation: principles and emerging applications," *Nanophotonics* **9**(12), 3755–3780 (2020).
27. J. Poirson, T. Lanternier, J.-C. Cotteverte, A. Le Floch, and F. Bretenaker, "Jones matrices of a quarter-wave plate for Gaussian beams," *Appl. Opt.* **34**(30), 6806–6818 (1995).
28. P.-N. Ni, P. Fu, P.-P. Chen, C. Xu, Y.-Y. Xie, and P. Genevet, "Spin-decoupling of vertical cavity surface-emitting lasers with complete phase modulation using on-chip integrated Jones matrix metasurfaces," *Nat. Commun.* **13**(1), 7795 (2022).
29. H. He, S. Tang, Z. Zheng, and F. Ding, "Multifunctional all-dielectric metasurface quarter-wave plates for polarization conversion and wavefront shaping," *Opt. Lett.* **47**(10), 2478–2481 (2022).

30. D. K. Cheng, *Field and wave electromagnetics* (Pearson Education India, 1989).
31. T.-Y. Huang, R. R. Grote, S. A. Mann, D. A. Hopper, A. L. Exarhos, G. G. Lopez, A. R. Klein, E. C. Garnett, and L. C. Bassett, "A monolithic immersion metalens for imaging solid-state quantum emitters," *Nat. Commun.* **10**(1), 2392 (2019).
32. J. L. Zhang, K. G. Lagoudakis, Y.-K. Tzeng, C. Dory, M. Radulaski, Y. Kelaita, K. A. Fischer, S. Sun, Z.-X. Shen, N. A. Melosh, S. Chu, and J. Vučković, "Complete coherent control of silicon vacancies in diamond nanopillars containing single defect centers," *Optica* **4**(11), 1317–1321 (2017).
33. H. Masuda, M. Watanabe, K. Yasui, D. Tryk, T. Rao, and A. Fujishima, "Fabrication of a Nanostructured Diamond Honeycomb Film," *Adv. Mater.* **12**(6), 444–447 (2000).
34. Y. Tao and C. Degen, "Facile Fabrication of Single-Crystal-Diamond Nanostructures with Ultrahigh Aspect Ratio," *Adv. Mater.* **25**(29), 3962–3967 (2013).
35. Y. S. Zou, Y. Yang, W. J. Zhang, Y. M. Chong, B. He, I. Bello, and S. T. Lee, "Fabrication of diamond nanopillars and their arrays," *Appl. Phys. Lett.* **92**(5), 1 (2008).